The Astrophysical Journal, 619:1132–1141, 2005 February 1

OXYGEN ABUNDANCE IN CORONAL STREAMERS

Alberto M. Vásquez[1]
Instituto de Astronomía y Física del Espacio, CC 67-Suc 28, (1428) Ciudad de Buenos Aires, Argentina; albert@iafe.uba.ar

and

John C. Raymond
Harvard-Smithsonian Center for Astrophysics, 60 Garden Street MS 15, Cambridge, MA 02138
Received 2004 February 6; accepted 2004 October 12

ABSTRACT

In a previous work we developed a stationary proton-electron MHD model of the solar corona, suitable for the minimum-activity epochs. In the present work, we use empirically derived information from the past solar minimum for the oxygen parameters (temperatures and outflow velocity) to develop an oxygen model in the frame of our previous model. *Solar and Heliospheric Observatory* UVCS observations of past minimum coronal streamers in the O VI λ1032 and O VI λ1037 lines have revealed that oxygen abundances are very much depleted within the stable closed-field regions of the quiescent streamers. This characteristic appears as a relatively dark region, often seen in the core of the quiescent equatorial streamers when imaged in oxygen lines. Using the oxygen abundance as a free parameter, we compute the expected O VI line emissivities from our models and synthesize images considering the projection effects in detail. We find here that, in order to obtain oxygen images with dark streamer cores similar to those observed, very low element abundances have to be assumed. The required depletion factors are lower than previous estimates that do not account for projection effects, which is especially important at 1.75 $R_\odot$ and higher.

Subject headings: solar wind — Sun: abundances — Sun: corona — Sun: UV radiation

1. INTRODUCTION

Elemental abundances in the solar atmosphere are not constant or uniform. Their study is important in itself and in connection with other issues of solar physics. They provide, for example, means to identify the coronal source of structures observed in the solar wind. Also, abundance determination affects the interpretation of many observations. As an example, emission measure determinations relying on narrowband EUV imaging (e.g., *SOHO* EIT, *TRACE*) depend on the assumed abundances, and the inferred temperatures can also depend on them (Ko et al. 2002).

Both stable and dynamic coronal structures present variations in their elemental abundances. The slow component of the solar wind shows important variations in its elemental fractional composition. The slow wind (and also active regions) exhibits the so-called first ionization potential (FIP) effect, a relative enhancement of low-FIP elements (those whose neutral species have an FIP below ~10 eV) with respect to high-FIP ones (Meyer 1985a, 1985b). Models for the FIP effect include those based on diffusion, magnetic field effects, preferential acceleration during reconnection events, and MHD wave effects (see J. C. Raymond 2005, in preparation, and references therein). Quiescent coronal streamers during minimum-activity epochs present elemental abundances that differ from photospheric values. Streamer observations during the past minimum in the O VI λ1032 and O VI λ1037 lines, performed with the Ultraviolet Coronagraph Spectrometer (UVCS) aboard the *Solar and Heliospheric Observatory* (*SOHO*; Kohl et al. 1995), have revealed that oxygen abundances are very much depleted within the stable closed-field regions of the quiescent streamers (Raymond et al. 1997b; Marocchi et al. 2001; Strachan et al. 2002; Uzzo et al. 2003). The observed depletions in the center of the streamers are a factor of the order of 10, and they are thought to be the result of gravitational settling (Raymond et al. 1997b; Feldman et al. 1999). An alternative explanation was proposed by Noci et al. (1997), suggesting that the streamer structure may be a multipolar structure so that open field lines could be located in the apparent center of the streamer. This scenario requires a smaller ion drag in the open field lines to explain the abundance depletion.

Wind elemental composition measurements are performed in situ by instruments aboard spacecraft, such as CELIAS/MTOF aboard *SOHO* (Hovestadt et al. 1995), SWICS aboard *Ulysses* (Bame et al. 1992), and SWEPAM aboard the *Advanced Composition Explorer* (*ACE*; McComas et al. 1998). On the other hand, abundances in coronal structures have to be inferred from UV spectral observations, such as those performed by UVCS and SUMER aboard *SOHO*. In this case, the abundance determination generally relies on ratios of collisionally excited UV emission lines. The observed intensities are the result of line-of-sight integrals. Even if for some structures the involved projection effects can be neglected, in general these have to be taken into account. For this, a three-dimensional model of the observed structure has to be assumed. Thus, UV morphological information on the region under study provided by EUV imagers such as *SOHO* EIT and *TRACE* is helpful.

The purpose of the present paper is to investigate oxygen abundance in streamer structures using a forward-modeling approach. We develop an oxygen model based on a previously developed minimum-corona model by Vásquez et al. (2003). We synthesize coronal images in the O VI λ1032 and O VI λ1037 lines considering projection effects in detail, which we find to be quite important at 1.75 $R_\odot$ and higher. In § 2 we describe our semiempirical models for the coronal magnetic structure and for the oxygen parameters (temperatures and outflow velocities). In § 3 we detail the formulae used for our UV emissivity computations. In § 4 we display the resulting images in the O VI

[1] Also at: Department of Physics, University of Buenos Aires, Argentina.

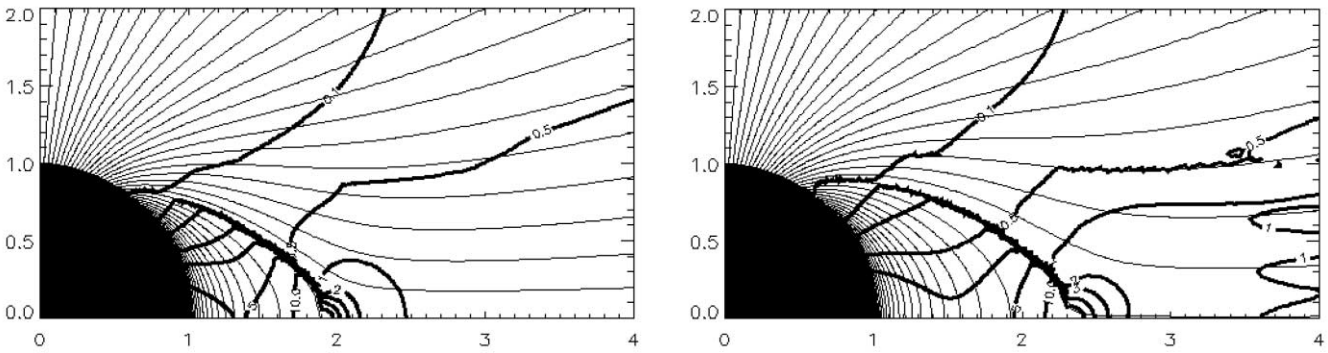

FIG. 1.—Magnetic fields (*thin lines*) and plasma-β contour plots of our models 1 (*left*) and 2 (*right*).

lines, synthesized from our models assuming different oxygen abundances, and we compare with *SOHO* UVCS observations. The main results of this work are discussed in § 5.

2. MODELS

In a previous work (Vásquez et al. 2003), we developed an MHD model for the minimum-activity global solar corona. Our models treat the macroscopic force balance of the global corona, accounting for (anisotropic) gas pressure, magnetic force, inertial effects, and gravity. Because of the assumed axisymmetry, the quantity $A = A_\phi r \sin(\theta)$ is a constant along each field line, where A_ϕ is the magnetic potential and r and θ are the radial and latitudinal coordinates, respectively. Using empirically derived constraints on density and temperature for protons and electrons, along both the pole and the equator, we model the transition of these quantities across field lines (i.e., as a function of A). We then solve the force balance, and as result we obtain models for the magnetic structure and the solar wind.

Our models depend on three free parameters, which are the fraction of the coronal base magnetic flux that is open, namely, A_c, the A value (i.e., the field line) for which the model of temperature across field lines takes its mean value, and the width in A values over which the temperature gradient across field lines takes place. In the present work, we show results for two configurations of our coronal model, differing only in the A_c value, which mainly affects the radial extent of the resulting streamer belt. The two configurations we use are

$$\text{Model 1}: \; A_c = 0.80 \rightarrow r_{\rm cusp} \sim 1.9 \; R_\odot,$$
$$\text{Model 2}: \; A_c = 0.70 \rightarrow r_{\rm cusp} \sim 2.3 \; R_\odot,$$

where $r_{\rm cusp}$ is the streamer belt cusp height (larger open-flux fractions decrease the streamer closed region height). Vásquez et al. (2003) show the full details for model configuration 1 and make detailed comparisons between white light and Lyα emissivity images synthesized from the model and past minimum observations. The magnetic field configurations and contours of plasma β are shown in Figure 1 for models 1 and 2.

In this work, we assume that the global corona structure is described by our electron-proton models 1 or 2, a few central aspects of which we point out now. As revealed by *SOHO* UVCS observations, proton and oxygen temperatures are characterized by thermal spreads that are larger in the perpendicular direction than in the parallel one. Hence, our temperature models 1 and 2 are characterized by strong anisotropies in the polar region. The density-enhanced streamer core region in the equator is modeled as a region with isotropic temperatures. The transition of temperatures from the polar to the equatorial region is done as a function of field line. Also, our velocity models 1 and 2 are characterized by bimodal wind solutions (Vásquez et al. 1999, 2003). Surrounding the streamer closed regions (or streamer core) is a slow-wind regime that arises from the model, which we call streamer legs. Along the open field lines of this region, the morphology of the streamer has an impact on the behavior of the wind solution. Below the streamer cusp, the subsonic outflow is decelerated and stagnated in its closest approach to the streamer cusp. Such a region of stagnated flow has been found previously by other authors (e.g., Wang 1994; Suess & Nerney 1999, 2002; Chen & Hu 2001). Outside that region, the wind solutions are different, belonging to a faster regime that here defines the polar hole region. We refer the reader to Vásquez et al. (2003) for a full description of the temperature and outflow velocity models.

For this work we developed a semiempirical oxygen model, based on our previous proton-electron model, in the following way. We refer to observational analyses of *SOHO* UVCS data of the past solar minimum that estimate both temperatures ($T_{\rm O}$) and outflow velocities ($V_{\rm O}$) of O^{5+} ions at the pole and equator. Those works also estimate proton temperatures (T_p) and velocities (V_p). We then compute the ratio between the observationally derived parameters for O^{5+} and those for the protons, and adopt those ratios for our model. Hence, in our model we set the O^{5+} parameters so that our modeled ratios, $T_{\rm O}/T_p$ and $V_{\rm O}/V_p$, equal those estimated from the observations.

The O^{5+} parallel temperatures are set equal to the proton parallel temperatures. For the larger O^{5+} perpendicular temperatures along the pole, we use the semiempirical results of Cranmer et al. (1999; their eqs. [19] and [28]) to set the $T_{\rm O}/T_p$ ratio, and then use our T_p model to infer a model for $T_{\rm O}$. For the O^{5+} perpendicular temperatures along the equator we do the same, but based on the results of Strachan et al. (2002) for streamers (see also Frazin 2002).

Following a similar approach for the O^{5+} outflow velocities, we infer plausible velocity profiles. For the polar region we refer to the results of Cranmer et al. (1999), showing oxygen outflow speeds of ~400 km s^{-1} at a height of 3 $R_\odot$. Comparable values are derived by other works such as Antonucci et al. (2004; 350–500 km s^{-1} at 3.1 $R_\odot$) and Giordano et al. (2000; 300 km s^{-1} at the same height). For outflow speed values representative of the streamer legs (the open field lines surrounding the streamer core and forming the streamer stalk above the cusp), we refer to Strachan et al. (2000, 2002). The former analyzes the latitudinal dependence of outflow speed during minimum at heights in the range 1.7–2.2 $R_\odot$ and the latter studies the outflow speed along the streamer axis, extending to heights above the cusp. Both works suggest that velocity values along the legs should increase up to ~100 km s^{-1} at a height located 1–2 $R_\odot$ above the streamer cusp. The works by

Strachan et al. (2000) and Habbal et al. (2001) analyze the latitudinal dependence of outflow speed near streamers. Both works show that a transition from higher to lower speeds occurs when approaching the streamer, within ~20° of the streamer axis. This is also a characteristic of the bimodal solutions in our models 1 and 2, as mentioned above.

We have applied the procedure previously described for models 1 and 2. In this way we obtain profiles for the O^{5+} temperatures and velocities at the pole and the equator. We then model the transition of the oxygen parameters across field lines in the same way as we do for our proton-electron temperature model (Vásquez et al. 2003).

We use the oxygen abundance as the main free parameter. As a guide, we take previous observational analyses of oxygen abundance in streamers. *SOHO* UVCS observations of past minimum coronal streamers in the O VI λ1032 and O VI λ1037 lines have revealed that oxygen abundances are very much depleted within the stable closed regions of the quiescent streamers (see, e.g., Raymond et al. 1997b; Parenti et al. 2000; Strachan et al. 2002; Uzzo et al. 2003). This appears as a relatively dark region in the core (as compared to the brightness on the streamer legs), often seen as a main characteristic in oxygen images of the quiescent equatorial streamers.

We thus model the oxygen abundance as a fraction of a typical photospheric quiet-Sun value, taken to be $A_{\rm O/H}^{\rm phot} = 8.55 \times 10^{-4}$ (Feldman 1992). We set the ratio $R_A \equiv A_{\rm O/H}/A_{\rm O/H}^{\rm phot}$ as a constant value that is separately chosen for different regions of the coronal structure described by our models 1 and 2. We set $R_A = 1$ in the polar hole region, $R_A = \frac{1}{3}$ along the streamer legs, and a variable fraction in the streamer core, ranging from $R_A = 1/10$ to $R_A = 1/100$. Finally, the O^{5+} concentration is consistently computed as a function of T_e from ionization balance calculations.

3. CORONAL UV EMISSIVITY

In general, coronal UV emission lines arise from both collisional and resonant excitation, and results depend not only on electron density and mean solar disk brightness but also on coronal ion parameters such as temperature, density, and bulk velocity (wind speed). The total intensity of the combined collisional and radiative (or resonantly) excited contributions, centered at a frequency ν, coming from an optically thin corona, is

$$I_\nu(\boldsymbol{n}) = I_\nu^{\rm coll} + I_\nu^{\rm res} = \int_{\rm LOS} dx\,(j_\nu^{\rm coll} + j_\nu^{\rm res}), \qquad (1)$$

where $\boldsymbol{n}$ is the unit vector directed along the line of sight (LOS; x-axis) and $j_\nu^{\rm coll}$ and $j_\nu^{\rm res}$ are the emissivities due to collisional and resonant excitation, respectively.

The resonant component of the line emissivity, in units of ergs cm^{-3} s^{-1} sr^{-1}, integrated in frequency around its central value ν_0, can be written as (Noci & Maccari 1999)

$$j_\nu^{\rm res} = \frac{h\nu_0}{4\pi} B_{12} N_g(Y^{+p}) \times \int_{\Omega'} d\omega' p(\boldsymbol{n}\cdot\boldsymbol{n}') \int d\boldsymbol{v} f(\boldsymbol{v}) I_\odot\left(\boldsymbol{n}', \nu_0 + \nu_0 \frac{\boldsymbol{v}\cdot\boldsymbol{n}'}{c}\right), \qquad (2)$$

where B_{12} ergs^{-1} s^{-1} cm^2 is the Einstein absorption coefficient for the considered transition and $N_g(Y^{+p})$ is the emitting ion's density. The exciting radiation propagation direction is indicated by $\boldsymbol{n}'$ and the corresponding solid angle integration extends over the solid cone Ω' subtended by the whole solar disk with respect to each point along the LOS. In general, the radiative scattering is not isotropic, and its direction-dependent probability is indicated by $p(\boldsymbol{n}\cdot\boldsymbol{n}')$. The velocity space integral couples the fraction of ions $d\boldsymbol{v} f(\boldsymbol{v})$ that have their velocity in the volume $d\boldsymbol{v}$ around $\boldsymbol{v}$, with the exciting disk intensity $I_\odot(\nu_0 + \nu_0 \boldsymbol{v}\cdot\boldsymbol{n}'/c)$ evaluated at the Doppler-shifted frequency able to excite that fraction of the ions in the frequency of the line of interest. Because of the Doppler shift effect, the effective exciting intensity seen by ions that have speed $\boldsymbol{v}$ decreases exponentially as $\boldsymbol{v}\cdot\boldsymbol{n}'$ increases, an effect known as Doppler dimming. The scattering probability has the general form $p = [a + b(\boldsymbol{n}\cdot\boldsymbol{n}')^2]/(4\pi)$ (Noci & Maccari 1999). For the case of the O VI λ1032 line, $a = \frac{7}{8}$ and $b = \frac{3}{8}$, and for the O VI λ1037 line $a = 1$ and $b = 0$. For our computations of both lines we have assumed the latter values, i.e., isotropic probability, which introduces errors on the order of 10% or less in the case of the O VI λ1032 line.

In this work we assume Maxwellian velocity distributions for the coronal ions. As indicated by the *SOHO* UVCS observations, the ions present anisotropic distributions. We then express the distribution as bi-Maxwellians and assume different thermal spreads for the directions parallel and perpendicular to the local magnetic field,

$$f(\boldsymbol{v}) = \frac{1}{(2\pi)^{3/2}\sigma_\parallel \sigma_\perp^2} \exp\left[-\frac{1}{2}\left(\frac{v_\parallel - w}{\sigma_\parallel}\right)^2\right] \exp\left[-\frac{1}{2}\left(\frac{v_\parallel}{\sigma_\perp}\right)^2\right], \qquad (3)$$

where w is the ion bulk outflow speed along the magnetic field. To compute the velocity and solid angle integrals, we assume isotropic exciting chromospheric profiles expressed as simple (or sums of) Gaussians, given by

$$I_\odot(\nu) = I_0 \exp\left[-\left(\frac{\nu - \nu_0}{\Delta\nu_I}\right)^2\right]. \qquad (4)$$

In the case of the O VI λ1032 line, the exciting profile consists of the corresponding solar disk O VI line centered at $\lambda =$ 1031.92 Å. For the O VI λ1037 line, in addition to the corresponding solar disk O VI line centered at 1037.61 Å, we also consider the effect of the neighboring C II lines centered at 1037.02 and 1036.34 Å. Because of the increasing Doppler shift for increasing outflow speeds, these two C II lines lead to a "Doppler pumping" effect. For the C II λ1037.02 line, the pumping is maximized when the outflow velocity is such that the wavelength of the C II photons, measured at the ions' moving frame, equals the rest-frame wavelength of the O VI λ1037 line, or ~175 km s^{-1}. For the C II λ1036.34 line, the maximum pumping outflow speed is 383 km s^{-1} (see also Dodero et al. 1998).

The collisional component of the line emissivity, in units of ergs cm^{-3} s^{-1} sr^{-1}, integrated in frequency around its central value ν_0, can be written as (Vásquez 2002)

$$j_\nu^{\rm coll} = \frac{h\nu_0}{4\pi} q_{gj}(T_e) B N_g(Y^{+p}) N_e, \qquad (5)$$

where B is the branching ratio for the considered transition, $q_{gj}(T_e)$ s^{-1} cm^3 is the collisional excitation rate coefficient and N_e is the electron's density. In both components of the total intensity, the emitting ion's density can be conveniently expressed as

$$N_g(Y^{+p}) = \frac{N_g(Y^{+p})}{N(Y)} A(Y) 0.8 N_e, \qquad (6)$$

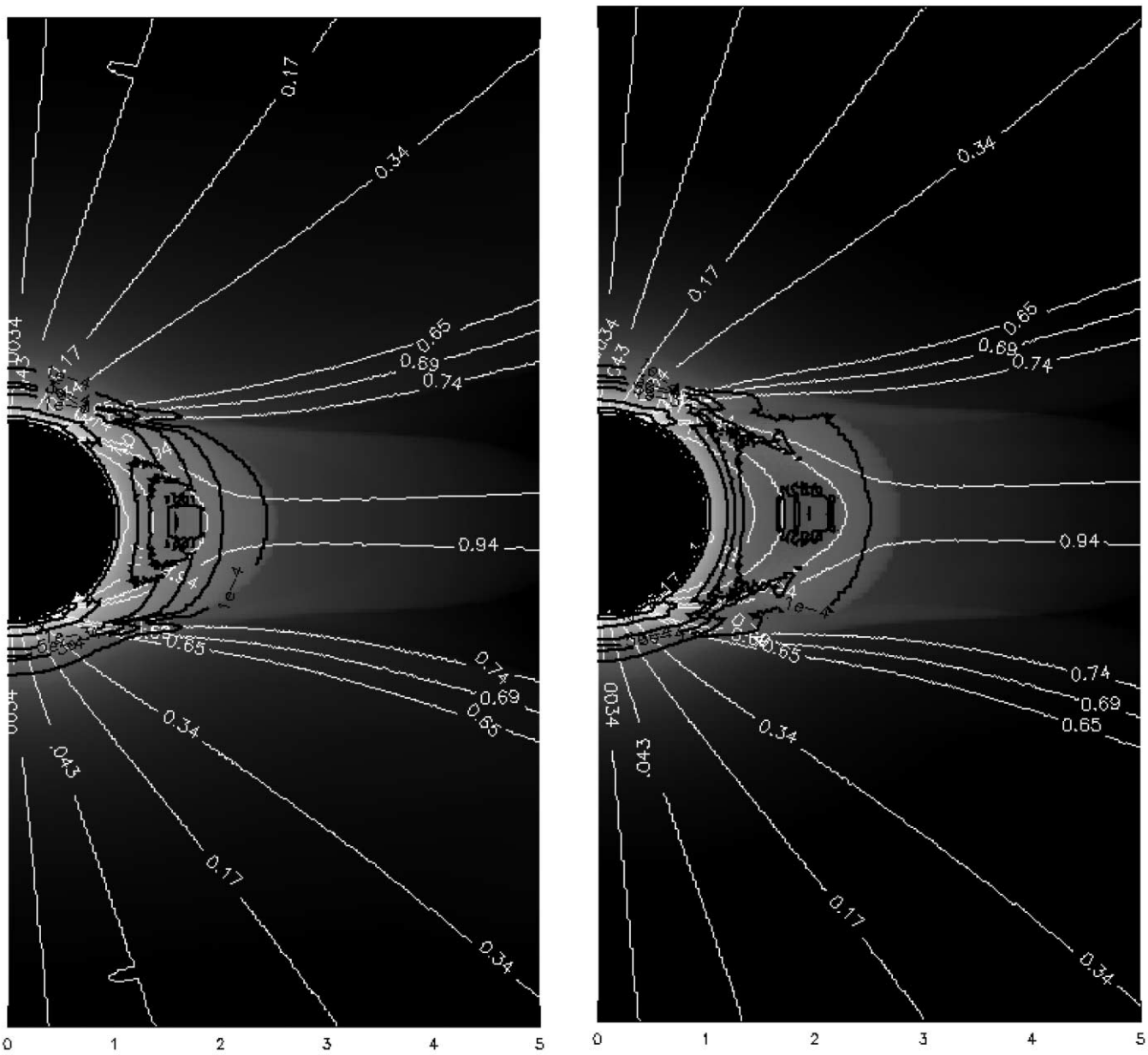

FIG. 2.—Artificial $\log_{10}(I_{\mathrm{O\,VI}\,\lambda1032})$ edge-on view (LOS in plane of equatorial current sheet), synthesized from our models 1 (*left*) and 2 (*right*). Both images were produced assuming that the oxygen abundance in the streamer closed region is depleted by a factor of 1/100. Black lines are contours of the same intensity with values $10^{-4}, 3\times10^{-4}, 5\times10^{-4}, 10^{-3}, 10^{-2}, 10^{-1}$, and 1 of the maximum intensity. White lines are selected magnetic field lines in the plane of the sky.

where $N(\mathrm{Y})$ is the density of the element Y, $A(\mathrm{Y}) \equiv N(\mathrm{Y})/N(\mathrm{H}^+)$ is the abundance of the element with respect to protons, the ratio $N_g(\mathrm{Y}^{+p})/N(\mathrm{Y})$ is the concentration of the emitting ion, and $0.8 \approx N(\mathrm{H}^+)/N_e$. The ion concentration is computed from ionization equilibrium calculations.

The assumption of ionization equilibrium may not apply during fast dynamical events, for which the temperature may evolve in timescales much shorter than those of ionization and recombination, a situation likely to occur in flares and in high-speed parts of the solar wind (Ko et al. 1997; Esser et al. 1998). On the other hand, ionization equilibrium seems a reasonable assumption for the relatively slowly evolving streamer core and streamer leg regions.

4. O VI IMAGES AND DERIVED ABUNDANCES

With our coronal models 1 and 2, described in § 2, and using equations (1)–(6), we can now synthesize images in the O VI lines. Most of the coronal UV lines observed by *SOHO* UVCS are mainly produced by collisional excitation. Nonetheless, the intense O VI lines contain comparable fractions of resonant and collisional components.

Assuming a fractional abundance of $R_A \equiv A_{\mathrm{O/H}}/A^{\mathrm{phot}}_{\mathrm{O/H}} = 1/100$ in the core of the streamer belt, $R_A = 1$ in the polar hole region, and $R_A = \frac{1}{3}$ along the streamer legs, Figure 2 shows resulting images in the O VI $\lambda1032$ line for models 1 and 2 in an edge-on view of the streamer belt (i.e., LOS in the plane of the equatorial current sheet). The white lines represent selected magnetic field lines of the model (in the plane of the sky), while the dark lines are contour levels of the O VI $\lambda1032$ intensity. The darker core is clearly seen in the results of both models 1 and 2.

For quantitative comparisons against solar minimum observations, Figure 3 shows latitudinal profiles, taken along a line perpendicular to the streamer axis (simulating the *SOHO* UVCS slit), for the two synthesized O VI $\lambda1032$ images at a

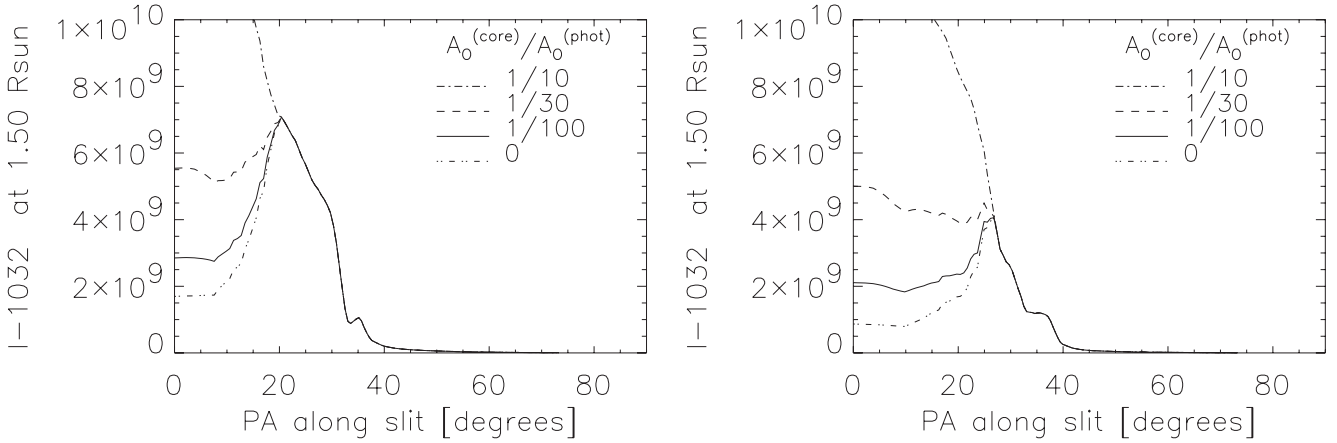

FIG. 3.—Artificial $I_{\text{O VI }\lambda1032}$ latitudinal profiles, synthesized from our models 1 (*left*) and 2 (*right*), assuming different oxygen abundances in the streamer closed region (core) relative to photospheric values. The profiles are taken along a line perpendicular to the streamer axis, at a height of 1.5 $R_\odot$ in both panels.

height of 1.5 $R_\odot$. Figure 4 shows the profiles for model 1 at 1.75 $R_\odot$ and for model 2 at 2.0 $R_\odot$, approximately the "center" of the streamer core in each case. For each model configuration, the different line styles represent the resulting profiles assuming different fractional abundances in the streamer core, $R_A = 0, 1/100,\ 1/30,$ and $1/10$. In all cases we keep the same fractional abundance along the streamer legs ($R_A = \frac{1}{3}$) and in the polar holes ($R_A = 1$). The line for zero oxygen abundance in the core has been computed to show the pure projection effect.

In a similar way, Figures 5 and 6 show the latitudinal profiles for the O VI $\lambda1037$ line. The radiative part of this line is Doppler pumped by the chromospheric C II radiation, an effect that is maximized when the oxygen ions outflow at a speed of ~175 km s^{-1}. For $R_A^{\text{core}} = 1/100$, the left panels of Figures 7 and 8 show the ratio $\Gamma = I_{\text{O VI }\lambda1032}/I_{\text{O VI }\lambda1037}$ for models 1 and 2, respectively. The right panels of Figures 7 and 8 show the outflow O^{5+} velocity V_O for both models, with the velocity contour $V_O \sim 175$ km s^{-1} indicated by a thick line. For zero or low enough outflow speeds, as in the streamer core and surrounding regions, the pumping effect is negligible and the intensity ratio ranges from $\Gamma \sim 2$, where collisions dominate, to $\Gamma \lesssim 4$, where the radiative excitation is dominant. In the polar region, and above $r > 2\ R_\odot$, outflow velocities are high enough for the radiative excitation to be less important, and there we get $\Gamma \sim 2$ (even if densities are very low). Regions where $\Gamma < 2$ (the darker region in the left panels of Figs. 7 and 8) indicate places where the C II pumping on the O VI $\lambda1037$ line is dominant. Comparing both panels of Figure 7 (model 1), we find that the region for which $\Gamma < 2$ surrounds the region where ions outflow almost radially at the speed that maximizes the C II pumping effect. Our results of $\Gamma > 2$ within the streamer core and stalk and $\Gamma < 2$ in the wind acceleration regions are in good agreement with the observational analysis of streamer by Strachan et al. (2002). The same behavior occurs for model 2, as shown in Figure 8.

To quantify the O VI $\lambda1032$ intensity contrast between the brighter legs and the darker core, in Table 1 we display, for $R_A = 1/100$, the peak intensity at the legs (I_{peak}) and the minimum intensity at the core (I_{core}), taken at the height of the streamer core center for each model. We also display different empirical values inferred from solar minimum observations of quiescent equatorial streamers. The synthesized $I_{\text{peak}}/I_{\text{core}}$ intensity contrast is in the range 2–3, similar to the observed values. For higher relative core abundances the dark core gets brighter. Assuming that $R_A = 1/30$, the intensity contrast drops to the range 1.5–2, and for $R_A = 1/10$ we do not get a dark core.

The collisional part of the measured intensities is given by the LOS integral of equation (5). As the coronal electron density decreases rapidly with height, that integral is dominated by the region closest to the photosphere. When looking at the denser

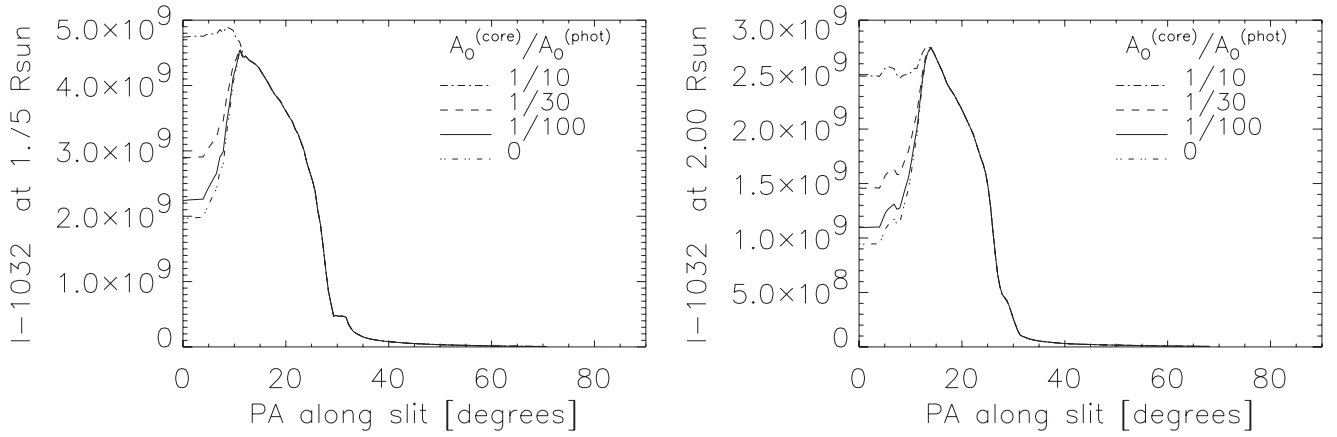

FIG. 4.—Artificial $I_{\text{O VI }\lambda1032}$ latitudinal profiles, synthesized from our models 1 (*left*) and 2 (*right*), assuming different oxygen abundances in the streamer closed region (core) relative to photospheric values. The profiles are taken along a line perpendicular to the streamer axis, at the height of the center of the streamer core, 1.75 $R_\odot$ (*left*) and 2.0 $R_\odot$ (*right*).

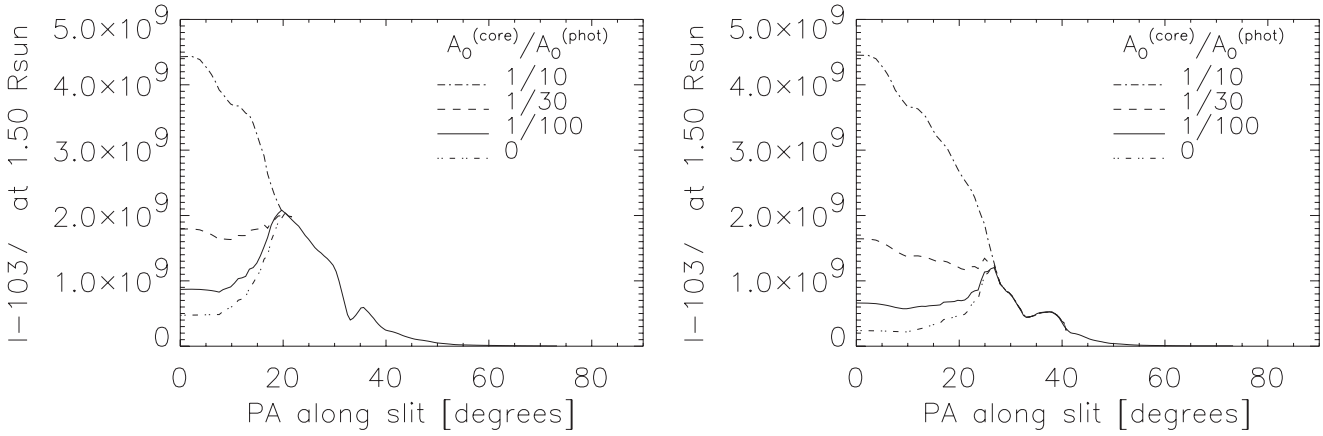

FIG. 5.—Artificial $I_{\mathrm{O\,VI}\ \lambda 1037}$ latitudinal profiles, synthesized from our models 1 (*left*) and 2 (*right*), assuming different oxygen abundances in the streamer closed region (core) relative to photospheric values. The profiles are taken along a line perpendicular to the streamer axis, at a height of 1.5 $R_\odot$ in both panels.

streamers in an edge-on view, we can therefore expect that the LOS integrals are dominated by the streamer core region. Therefore, previous streamer observational works (Raymond et al. 1997b; Marocchi et al. 2001; Uzzo et al. 2003) estimate the oxygen abundance by approximating the LOS collisional integral by its part located in the streamer core, to obtain

$$A_{\mathrm{O/H}} = \frac{I^{\mathrm{coll}}_{1032}}{I^{\mathrm{coll}}_{\mathrm{Ly}\beta}} \frac{B_{\mathrm{Ly}\beta}}{B_{\mathrm{O\,VI}}} \frac{C_{\mathrm{H\,I}}}{C_{\mathrm{O\,VI}}} \frac{q_{\mathrm{Ly}\beta}}{q_{\mathrm{O\,VI}}}, \tag{7}$$

where the "X" ion concentration $C_{\mathrm{X}}(T_e)$ and the collisional excitation rate $q_{\mathrm{X}}(T_e)$ are evaluated at the estimated temperature of the streamer core. Taking the collisional part of our model-synthesized images and the streamer core values of our electron temperature model, we infer the oxygen abundance at the streamer core using equation (7), i.e., assuming that the intensities are a LOS average. In Table 1 we display the results of applying this approach to our synthesized images at the streamer core center, as well as observational values. We report the results normalized to the photospheric abundance, using as a representative value $A^{\mathrm{phot}}_{\mathrm{O/H}} = 8.55 \times 10^{-4}$ (Feldman 1992). It can be seen that the core abundance values inferred from the synthesized images using equation (7) are similar to the observational results. We also note that, for both model configurations, the abundances inferred in this way are higher than the values assumed in the models. For example, in the second line of Table 1 the inferred abundance is $[A_{\mathrm{O/H}}]/[A_{\mathrm{O/H}}]^{\mathrm{phot}} \sim 0.05$. Having set this value at 0.01, the inferred overestimation is purely attributable to projection effects. In Figure 9 we show how the inferred abundances vary with height along the equator. The top panel shows the collisional part of the O VI λ1032 intensity, and the bottom panel shows the abundance inferred from these profiles (as well as those for Lyβ) applying equation (7). The dashed lines indicate the reference heights 1.75 and 2.05 $R_\odot$, for models 1 and 2, respectively, at which the streamer core looks dimmer in the O VI lines. The projection effect is especially important at 1.75 $R_\odot$ and higher. We thus suggest that the observational estimates that do not account for projection effects have to be taken as upper bounds and that oxygen abundance depletion can be stronger than previously estimated.

To quantify the projection effect in more cases, we have assumed different abundances in the streamer core and then applied equation (7) to the resulting images to infer the core abundance. Table 2 shows, for models 1 and 2, the results assuming the core abundances (relative to the photospheric level) 1/100, 1/30, and 1/10. It can be seen that the inferred

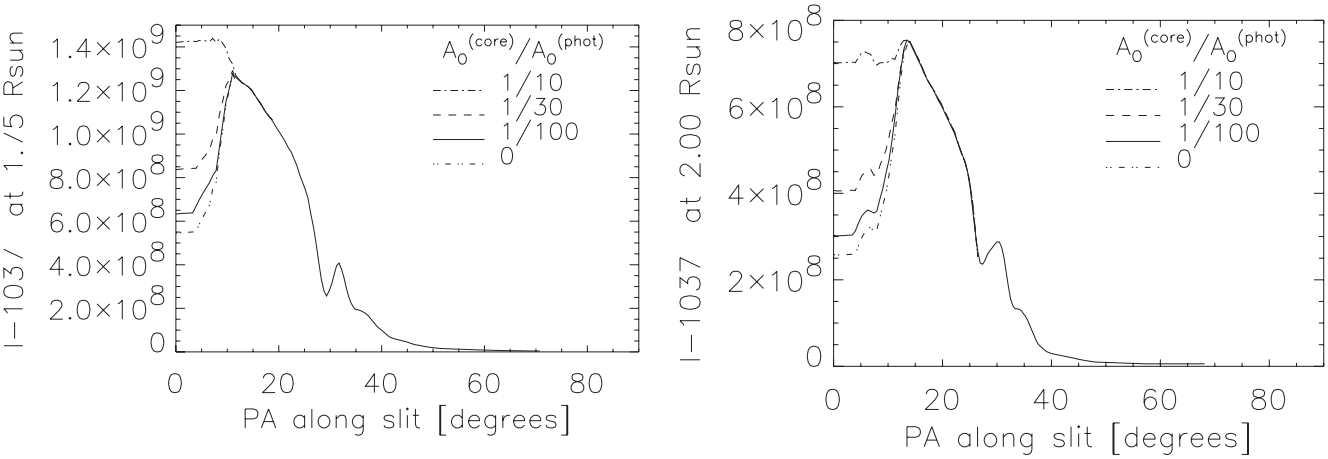

FIG. 6.—Artificial $I_{\mathrm{O\,VI}\ \lambda 1037}$ latitudinal profiles, synthesized from our models 1 (*left*) and 2 (*right*), assuming different oxygen abundances in the streamer closed region (core) relative to photospheric values. The profiles are taken along a line perpendicular to the streamer axis, at the height of the center of the streamer core, 1.75 $R_\odot$ (*left*) and 2.0 $R_\odot$ (*right*).

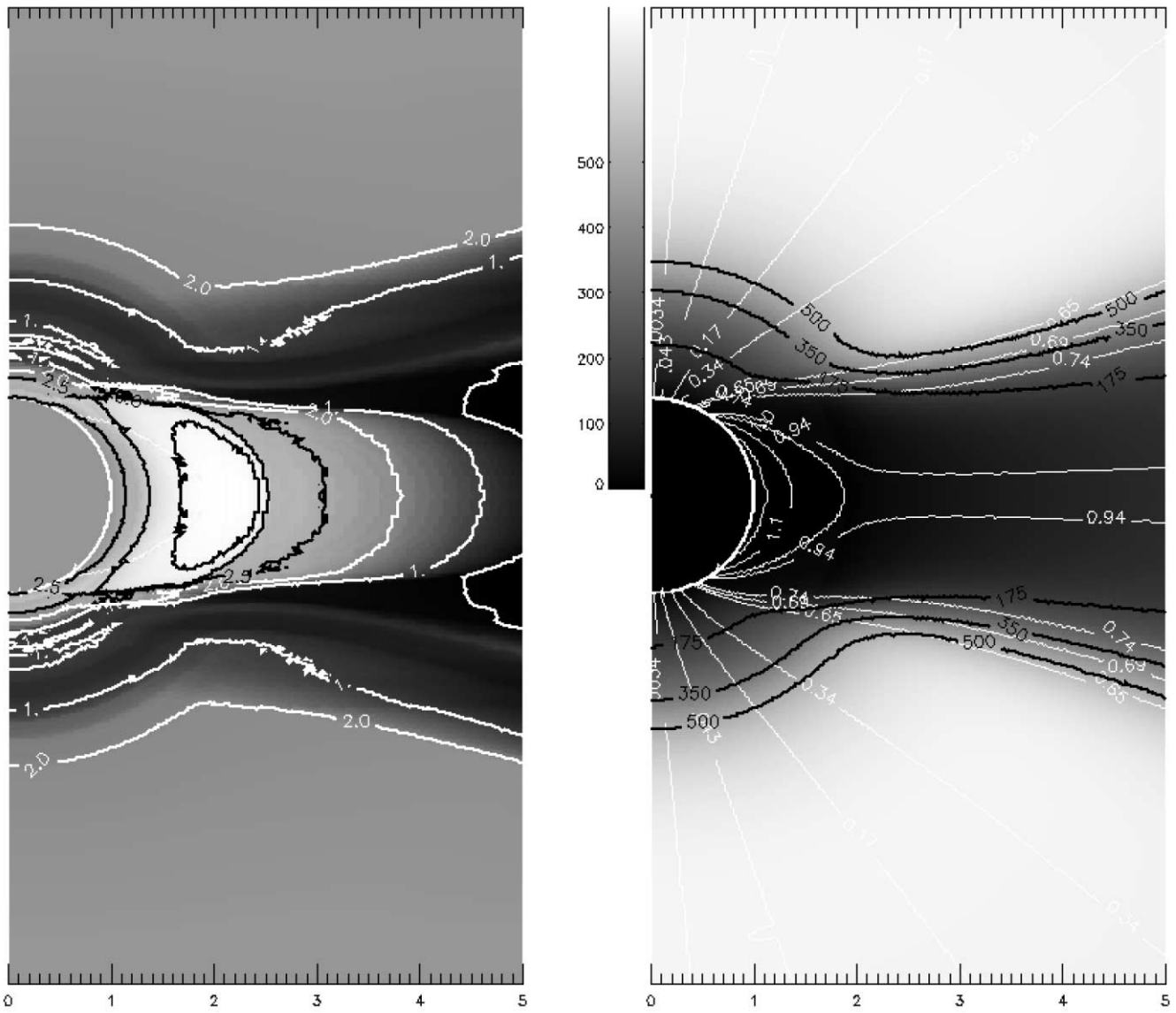

FIG. 7.—*Right*: Ratio $\Gamma = I_{\mathrm{O\ VI}\ \lambda1032}/I_{\mathrm{O\ VI}\ \lambda1037}$, synthesized from our model 1, assuming that the oxygen abundance in the streamer closed region is depleted by a factor of 1/100. Higher values of the ratio are brighter and lower values are darker, with contour plots (*thick lines*) of values $\Gamma = 0.25$, 1.0, 2.0, 2.5, 3.0, and 3.5. *Left*: Outflow O^{5+} velocity V_O in km s^{-1}. Regions where $\Gamma < 2$ surround the outflow velocity contour $V_O \sim 175$ km s^{-1} (indicated as a contour plot in the right panel), for which the C II λ1037.02 line pumping effect on the O VI λ1037 line is maximized. This region extends up to the region where velocities reach ~380 km s^{-1}, for which the pumping by the C II λ1036.34 line is maximized. Thin white lines are selected magnetic field lines in the plane of the sky.

abundances are systematically larger than the assumed values, the difference being more significant for lower abundances. Comparing the observed values of Table 1 with the inferred values in Table 2, we find that our synthesized images are consistent with observations if core abundances are depleted (relative to the photospheric value) by a factor between 1/100 and 1/30.

The corresponding latitudinal profiles are shown in Figure 4. As discussed above, the profiles for $R_A = 1/100$ and $1/30$ are consistent with observations, while the profile for $R_A = 1/10$ does not show a dark core. In Vásquez et al. (2003) we have shown detailed white-light and Lyα emissivity computations from our models. The consistency of those results with past minimum observations (Cranmer et al. 1999; Gibson et al. 1999; Guhathakurta et al. 1999) shows that the electron densities of our models are consistent with typical solar minimum conditions. Using the same model configuration, we find here that we need to assume very much depleted oxygen abundances to obtain O VI λ1032 images with darker streamer cores. It seems then that the electron density contrast between the streamer core and legs is high enough that very low oxygen abundances in the core are needed in order to see a central darker feature.

Finally, we compare with our calculations for zero core abundance. At 1.75 $R_\odot$ and higher, there is an almost negligible difference between the images of the 0 and 1/100 abundance models at the center of the streamer (see Figs. 4 and 6). This indicates that the projected emission from the streamer legs completely dominates for this very low abundance value. At the same heights and also in the center of the streamer, there is a contrast of a factor of the order of 2 between the images of the 0 and 1/30 abundance models, so in this case about half of the observed intensity is due to projection effects. At a lower height, specifically at 1.5 $R_\odot$ (see Figs. 3 and 5), the contrast between the images of the zero core abundance model and those of the 1/30 and 1/100 abundance models is clearly larger, indicating

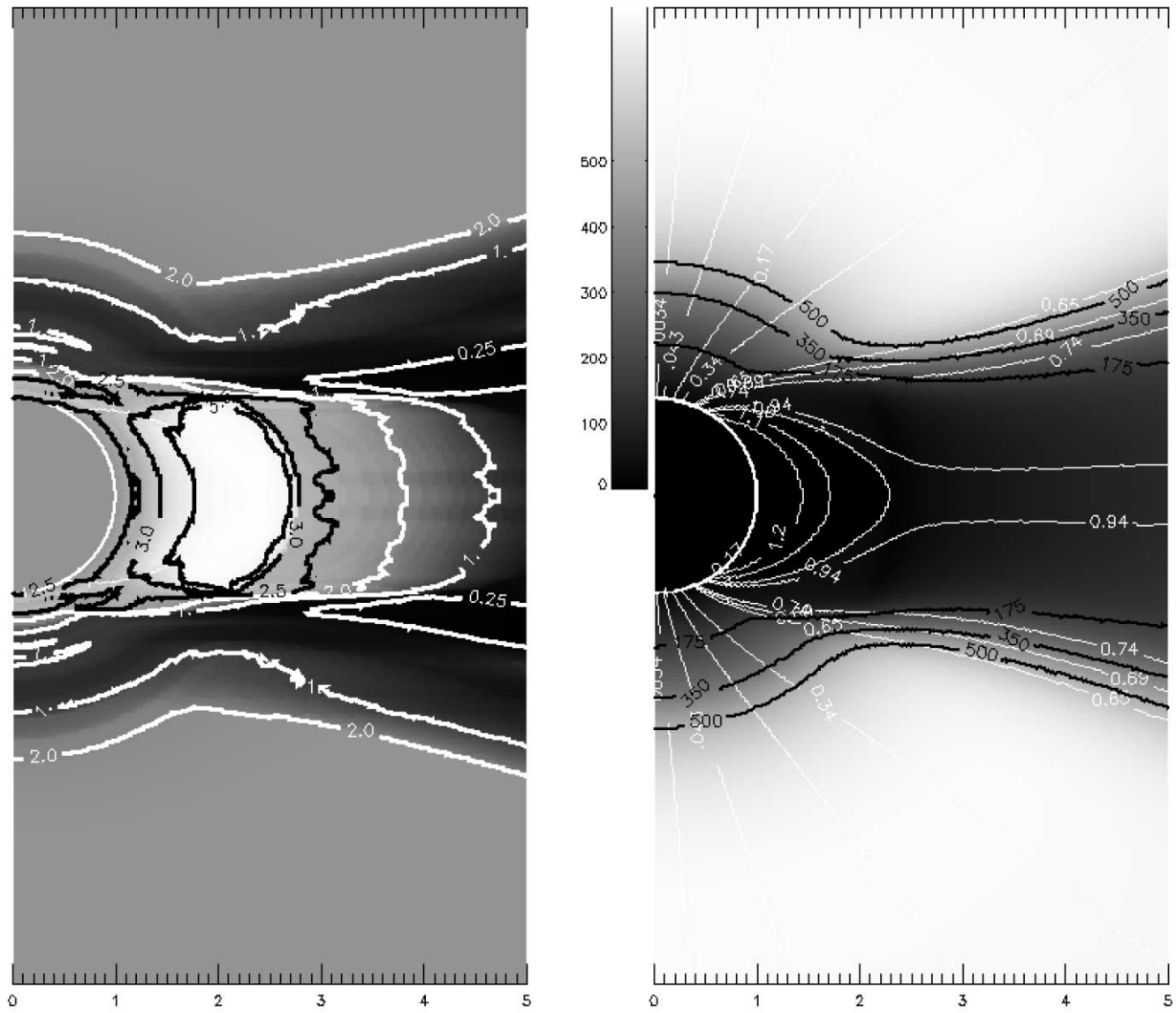

FIG. 8.—Same as Fig. 7, but synthesized from our model 2, assuming that the oxygen abundance in the streamer closed region is depleted by a factor of 1/100.

that the profiles depend more directly on the assumed abundance and that projection effects are weaker at lower heights.

5. DISCUSSION AND CONCLUSIONS

Using our semiempirical models for the proton-electron global corona (Vásquez et al. 2003), and on the basis of empirical constraints on oxygen ions (Cranmer et al. 1999; Strachan et al. 2002), we develop coronal oxygen models suitable for solar minimum conditions.

With configurations of our models that are consistent with observational constraints (white-light and Lyα images), we use the oxygen abundance as a free parameter to produce synthesized O VI λ1032 and O VI λ1037 images. We show that in order to obtain dark streamer cores (relative to the surroundings), very low abundances have to be assumed. The abundance in the streamer cores could be depleted (relative to photospheric values) by a factor ranging from 1/30 to 1/100. We also find that, for these low abundances and at 1.75 $R_\odot$ and higher, there is a relatively low intensity contrast (less than a factor of 2) between the corresponding synthesized images. This indicates that, for very low abundance models, the images are dominated by the projected emission from the streamer legs at those heights. At lower heights (1.5 $R_\odot$) we find that the contrast between the corresponding synthesized images increases up to a factor of order 3, indicating that projection effects are weaker at lower heights. The projection effect alone was quantified assuming a zero core abundance model. At heights 1.75 $R_\odot$ and larger, we find that half or more of the observed intensity comes from projection effects, while at heights of the order of 1.5 $R_\odot$ these are much weaker. Taking this into account, the similar abundances inferred for a past minimum streamer at heights 1.5 and 1.7 $R_\odot$ (see Table 1, observations by Raymond et al. 1997b and Uzzo et al. 2003) suggests that the oxygen abundance decreases with height. Marocchi et al. (2001) report a decline in streamer leg abundances with height. However, the apparent decline could be partly due to a projection effect, in that (as shown above) it is difficult to separate core and leg contributions at the larger heights, and contamination of their streamer leg spectra by Lyβ emission from the core would produce an artificially low oxygen abundance.

Previous observational analyses (Raymond et al. 1997b; Marocchi et al. 2001; Uzzo et al. 2003) have already indicated

TABLE 1
O VI λ1032 STREAMER INTENSITIES FROM MODEL-SYNTHESIZED IMAGES AND OBSERVATIONS

Model/Observation	I_{peak} (photons cm^{-2} s^{-1} sr^{-1})	I_{core} (photons cm^{-2} s^{-1} sr^{-1})	$A_{O/H}$	$A_{O/H}/A_{O/H}^{phot}$
Synthesized Images				
Model 1, at 1.75 $R_\odot$	4.5×10^9	2.2×10^9	3.4×10^{-5}	0.04
Model 2, at 2.00 $R_\odot$	2.7×10^9	1.1×10^9	3.9×10^{-5}	0.05
Raymond et al. (1997b) Observations				
1996 Jul 26, at 1.5 $R_\odot$	8.2×10^9	3.7×10^9	5.2×10^{-5}	0.06
Uzzo et al. (2003) Observations				
1996 Jun 26, at 1.7 $R_\odot$	8.0×10^9	3.0×10^9	4.8×10^{-5}	0.06
Marocchi et al. (2001) Observations				
1996 Apr 11, at 1.7 $R_\odot$	3.5×10^9	1.5×10^9	2.9×10^{-5}	0.04
1996 Jun 5, at 1.7 $R_\odot$	...	...	5.6×10^{-5}	0.07
Strachan et al. (2002) Observations				
1997 Apr 23, at 2.3 $R_\odot$	6.0×10^8	2.0×10^8	...	...

NOTES.—O VI λ1032 streamer intensities from model-synthesized images and observations. Intensities at the streamers' legs (I_{peak}) and core (I_{core}), and oxygen abundances ($A_{O/H}$) derived with eq. (7).

that minimum oxygen abundance values in streamer cores are depleted by at least 1 order of magnitude with respect to photospheric levels. Our forward-modeling calculations, which consider projection effects in detail, suggest that those estimates should be taken as upper bounds, and more extreme reduction factors could be expected. Raymond et al. (1997a) used a semiempirical model to investigate the projection effects for the quiet-Sun equatorial streamer. They found that the streamer legs contributed ~20%, 50%, and 80% of the O VI intensity at the center of the streamer at heights of 1.5, 1.75, and 2 $R_\odot$, respectively. The present results are approximately consistent with these estimates because our streamer model was chosen to fit the same streamer observations. In general, the contribution of the streamer legs to the apparent brightness of the streamer core will be sensitive to the height of the cusp and to the inclination of the streamer to the line of sight. Especially at heights above 1.7 $R_\odot$, projection effects should not be ignored. The forward-modeling approach described here or tomographic reconstruction of the three-dimensional structure of the streamer, as employed by Strachan et al. (2000), is necessary to derive reliable elemental abundances and outflow speeds.

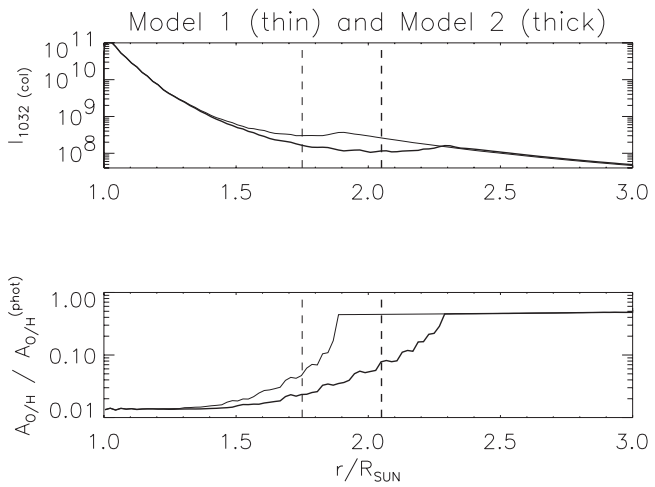

FIG. 9.—*Top*: Collisional part (for models 1 and 2) of the O VI λ1032 intensity along the equator. *Bottom*: Abundance inferred from these profiles (as well as those for Lyβ) applying eq. (7). For the results of both model 1 and model 2, we assumed that the streamer closed region oxygen abundance is depleted by a factor of 1/100. The departure of the inferred values from that number is due to projection effects, which become especially important at 1.75 $R_\odot$ and higher.

Accurate abundances are particularly important for the identification of the sources for the slow component of the solar wind, which is always observed in connection with streamer structures. The observational streamer oxygen abundance analysis by Raymond et al. (1997b) and Marocchi et al. (2001) found that the typical abundance of oxygen is a factor of 3–5 lower in the streamer cores than in the slow wind. That conclusion strongly indicates that the slow-wind plasma is not mainly fed by release of material trapped in the cores (by magnetic reconnection). More probably it is channeled out by open regions surrounding the streamers. If, as we suggest, those previous streamer core abundances are to be taken as upper bounds, the difference from the wind composition may be even larger than previously estimated. This would stress even more the difference in composition between the core-trapped material and that forming the slow wind.

TABLE 2
ASSUMED AND DERIVED ABUNDANCES AT STREAMER CORE

Model Configuration	Assumed Abundance	Inferred Abundance
M1 at 1.75 $R_\odot$	0.01	0.04
	0.03	0.06
	0.10	0.12
M2 at 2.0 $R_\odot$	0.01	0.05
	0.03	0.07
	0.10	0.13

NOTES.—Assumed and derived abundances at streamer core for model 1 (M1) at 1.75 $R_\odot$ and for model 2 (M2) at 2.0 $R_\odot$. Abundances are indicated as fractions of the assumed photospheric value.

We express our gratitude to the anonymous referee for a critical reading of the manuscript and very useful suggestions. We also thank Adriaan van Ballegooijen for helpful comments on this manuscript. This work was funded by the Smithsonian Astrophysical Observatory (US) under NASA grant NAG5-11420 and by the Consejo Nacional de Investigaciones Científicas y Técnicas (CONICET-Argentina). We also thank Fundación Antorchas (Argentina) for its support through grant 14056-20.

REFERENCES

Antonucci, E., Dodero, M. A., Giordano, S., Krishnakumar, V., & Noci, G. 2004, A&A, 416, 749
Bame, S. J., McComas, D. J., Barraclough, B. L., Phillips, J. L., Sofaly, K. J., Chavez, J. C., Goldstein, B. E., & Sakurai, R. K. 1992, A&AS, 92, 237
Chen, Y., & Hu, Y. Q. 2001, Sol. Phys., 199, 371
Cranmer, S. R., et al. 1999, ApJ, 511, 481
Dodero, M. A., Antonucci, E., Giordano, S., & Martin, R. 1998, Sol. Phys., 183, 77
Esser, R., Edgar, R. J., & Brickhouse, N. S. 1998, ApJ, 498, 448
Feldman, U. 1992, Phys. Scr., 46, 202
Feldman, U., Doschek, G. A., Schüle, U., & Wilhelm, K. 1999, ApJ, 518, 500
Frazin, R. A. 2002, Ph.D. thesis, Univ. Illinois, Urbana-Champaign
Gibson, S. E., Fludra, A., Bagenal, F., Biesecker, D., Del Zanna, G., & Bromage, B. 1999, J. Geophys. Res., 104, 9691
Giordano, S., Antonucci, E., & Dodero, M. A. 2000, Adv. Space Res., 25, 1927
Guhathakurta, M., Fludra, A., Gibson, S. E., Biesecker, D., & Fisher, R. 1999, J. Geophys. Res., 104, 9801
Habbal, S. R., Woo, R., & Vial, J.-C. 2001, Space Sci. Rev., 97, 5
Hovestadt, D., et al. 1995, Sol. Phys., 162, 441
Ko, Y.-K., Fisk, L. A., Geiss, J., Gloeckler, G., & Guhatakurtha, M. 1997, Sol. Phys., 171, 345
Ko, Y.-K., Raymond, J., Li, J., Ciaravella, A., Michels, J., Fineschi, S., & Wu, R. 2002, ApJ, 578, 979
Kohl, J. L., et al. 1995, Sol. Phys., 162, 313
Marocchi, D., Antonucci, E., & Giordano, S. 2001, Ann. Geophys., 19, 135
McComas, D. J., Bame, S. J., Barker, P., Feldman, W. C., Phillips, J. L., Riley, P., & Griffee, J. W. 1998, Space Sci. Rev., 86, 563
Meyer, J. P. 1985a, ApJS, 57, 151
———. 1985b, ApJS, 57, 173
Noci, G., & Maccari, L. 1999, A&A, 341, 275
Noci, G., et al. 1997, in Proc. 5th *SOHO* Workshop: The Corona and Solar Wind Near Minimum Activity, ed. A. Wilson (ESA SP-404; Noordwijk: ESA), 75
Parenti, S., Bromage, B. J. I., Poletto, G., Noci, G., Raymond, J. C., & Bromage, G. E. 2000, A&A, 363, 800
Raymond, J. C., Suleiman, R., van Ballegooijen, A., & Kohl, J. 1997a, Proc. 31st ESLAB Symp., Correlated Phenomena at the Sun, in the Heliosphere and in Geospace, ed. A. Wilson (ESA SP-415; Noordwijk: ESA), 383
Raymond, J. C., et al. 1997b, Sol. Phys., 175, 645
Strachan, L., Panasyuk, A. V., Dobrzycka, D., Kohl, J. L., Noci, G., Gibson, S. E., & Biesecker, D. A. 2000, J. Geophys. Res., 105, 2345
Strachan, L., Suleiman, R., Panasyuk, A. V., Biesecker, D. A., & Kohl, J. L. 2002 ApJ, 571, 1008
Suess, S. T., & Nerney, S. F. 1999, in Proc. 9th European Meeting on Solar Physics, Magnetic Fields and Solar Processes, ed. A. Wilson (ESA SP-44; Noordwijk: ESA), 1101
———. 2002, ApJ, 565, 1275
Uzzo, M., Ko, Y.-K., Raymond, J. C., Wurz, P., & Ipavich, F. M. 2003, ApJ, 585, 1062
Vásquez, A. M., 2002, Ph.D. thesis, Univ. Buenos Aires
Vásquez, A. M., van Ballegooijen, A. A., & Raymond, J. C. 1999, in AIP Conf. Proc. 471, Solar Wind Nine: Proc. Ninth Int. Solar Wind Conf., ed. S. R. Habbal et al. (Woodbury: AIP), 243
———. 2003, ApJ, 598, 1361
Wang, Y.-M. 1994, ApJ, 437, L67